Applying Model-Free Predictive Current Control With Parallel Cost Functions for Open-End Winding Synchronous Reluctance Motor

Mahdi S. Mousavi, Behnam Nikmaram, Abolfazl Nassaji, S. Alireza Davari, *Senior Member, IEEE*, Freddy Flores-Bahamonde, *Senior Member, IEEE*, and Jose Rodriguez, *Life Fellow, IEEE*

***Abstract*—This article presents a model-free predictive current control (MFPCC) with parallel cost functions for the common dc-link dual-inverter-fed open-end winding synchronous reluctance motor (OW-SynRM). The MFPCC has a general prediction algorithm that can be implemented in any reference frame. Using this feature, and the fact that each winding of the OW-SynRM is supplied separately by two legs of the dual inverter, the current predictions are achieved independently for each phase in the Cartesian coordinates. Then, three parallel cost functions are defined for three predicted phase currents. Thus, the finite control-set approach is utilized separately for each phase to determine the switching state of the dual inverter. In addition, an adaptive proportional-resonant extended state observer (PR-ESO) is introduced to improve the current predictions regarding the operating frequency of the motor. The proposed MFPCC for OW-SynRM has several advantages. First, the computational burden is decreased significantly because the prediction algorithm utilizes fewer candidates in the Cartesian coordinates. In addition, the weighting factor is not required due to using independent cost functions. Furthermore, the zero sequence current is automatically adjusted without a controller. Finally, the PR-ESO-based model-free approach improves the current predictions of the proposed method. The proposed MFPCC of the OW-SynRM is evaluated using the experimental results.**

***Index Terms*—Finite control-set model predictive control (FCS-MPC), model-free, open-end winding, predictive control, resonant observer, synchronous reluctance motor, zero sequence current (ZSC).**

Received 24 September 2024; revised 19 December 2024; accepted 20 January 2025. Date of publication 24 January 2025; date of current version 26 February 2025. The work of Freddy Flores-Bahamonde was supported by the Agencia Nacional de Investigacion y Desarrollo (ANID) under SERC Chile Grant ANID/FONDAP/1522A0006. The work of Jose Rodriguez was supported by the ANID through Project FB0008 under Grant 1210208 and Grant 1221293. This work was supported by the Shahid Rajaee Teacher Training University under Grant 5973/77. Recommended for publication by Associate Editor J. Ye. *(Corresponding author: S. Alireza Davari.)*

Mahdi S. Mousavi, Behnam Nikmaram, and S. Alireza Davari are with the Department of Electrical Engineering, Shahid Rajaee Teacher Training University, Tehran 16788, Iran (e-mail: davari@sru.ac.ir).

Abolfazl Nassaji is with the Department of Electrical Engineering, University of Science and Culture, Tehran 1461968151, Iran.

Freddy Flores-Bahamonde is with the Faculty of Engineering, Universidad Andres Bello, Santiago 8370146, Chile.

Jose Rodriguez is with the Faculty of Engineering, Universidad San Sebastian, Santiago 7550196, Chile.

Color versions of one or more figures in this article are available at https://doi.org/10.1109/TPEL.2025.3533562.

Digital Object Identifier 10.1109/TPEL.2025.3533562

I. Introduction

OPEN-END winding motor (OWM) drives fed by dual inverters have gained significant attention in electric vehicles (EVs) due to features, such as superior fault-tolerant capabilities and improved dc-link utilization [1], [2], [3]. With higher dc-link utilization, dual inverter drives can deliver equivalent torque to a typical single-inverter drive while operating at only half the dc-link voltage. This reduces voltage stress on each switch, decreases the number of required battery cells, and enables the use of lower-ratio boost dc–dc converters in EVs. In addition, dual inverters offer more flexible and reliable operation, thanks to their fault-tolerant design [3], [4].

On the other hand, recent advancements in rotor shape design [5] have increased interest in synchronous reluctance motors (SynRMs) as an alternative to induction motors (IMs) and permanent magnet synchronous motors (PMSMs) [6]. SynRMs are more efficient than IMs due to reduced rotor losses and lower operational temperatures [7]. Compared to PMSMs, SynRMs are more cost-effective and reliable since they do not require magnet [8]. In [7], a thorough comparison of material costs for manufacturing SynRMs, IMs, and interior PMSMs (IPMSMs) revealed that the cost of SynRM is about 33% lower than that of the IPMSM and 23% lower than that of the IM. The high reliability, combined with low cost, makes SynRMs an excellent candidate for EVs.

Therefore, implementing SynRM drives within a dual inverter structure can create a highly reliable drive system. This integration—dual-inverter-fed open-end winding SynRM (OW-SynRM) drive—offers significant advantages for demanding applications, such as EVs and high-performance industrial systems. However, few studies have explored this structure [9], [10], [11]. Thus, this article selects the OW-SynRM as the subject motor to investigate its proposed control for OWM drives.

In the dual inverter, two voltage source inverters (VSIs) feed the OWM, one VSI on each side of the winding. These two VSIs can be supplied in three different ways as follows: 1) by two isolated dc sources [12], 2) by a common dc source [13], and 3) by a dc source on one side and a floating capacitor on the other side [14].

Using a single dc source rather than two isolated sources reduces the cost of the dual inverter. However, this configuration leads to the circulation of the zero-sequence current

(ZSC) generated by the common mode voltage [15]. The ZSC should be suppressed otherwise it increases torque ripple and motor losses. To this end, several studies have been conducted to mitigate ZSC in OWM drives. A hysteresis controller has been employed in [16] and[17] to eliminate the ZSC. Also, the proportional resonant controller and a modified space vector pulsewidth modulation (SVPWM) have been employed together in [18] for this purpose. In [19], the projections of the ZSC on the rotating dq frame have been detected and suppressed by the proportional–integral (PI) controllers. Despite using different controllers, these methods have the same implementation approach, which is the modification of the SVPWM by the controller's output signal. These modifications complicate the implementation process.

In the finite control-set model predictive control (FCS-MPC), which does not require a modulation unit, the ZSC suppression is more straightforward. In this approach, the ZSC can be added as a controlled variable to the cost function [20]. This technique requires ZSC prediction for each feasible voltage vector.

Notably, the common dc source dual inverter has a 3-D space vector diagram with 27 different voltage vectors (VVs) in the stationary frame [20]. The high number of VVs complicates the switching algorithm, either direct or modulation-based switching methods. This is another issue of this configuration that should be addressed. For this objective, many studies have been conducted in the literature [17], [20], [21], [22], [23], [24].

The simplification techniques of direct switching algorithms, such as FCS-MPC, which is the focus of this article, can be categorized into two groups. The first group reduces the candidate VVs by classifying them according to the state of a controlled variable, such as ZSC [21], [25], voltage angle [20], electromagnetic torque error [23], and motor speed [24]. While this strategy reduces the computational burden of FCS-MPC in OWM drives, the reduced VV candidates affect the overall performance of the system. The second group performs the prediction algorithm consecutively for each side of the dual inverter [26], [27], [28]. Unlike the first group, this strategy does not require additional knowledge of a certain variable. Also, it is possible to remove the weighting factors [28]. Even though the second group achieves a low computational burden without categorizing the VVs, it should be noted that these methods prioritize the ZSC over the other controlled variables [26], [27].

To address the mentioned problems, this article presents a new predictive control architecture for the common dc source dual inverter, which is used to drive an OW-SynRM. The proposed method inherently requires low computational effort, rather than merely attempting to reduce the computational burden of existing predictive algorithms for dual-inverter-fed OWM drives. This inherent low computational requirement is achieved by exploiting the model-free predictive current control (MFPCC) theory. In addition to the well-known model-independent feature of MFPCC, which has been widely studied in various applications [29], [30], [31], it offers another significant advantage: a generalized formulation. This feature allows the predictive algorithm to operate in the Cartesian frame, similar to the approach used in [32] for multiphase drives. By leveraging this capability in the proposed method, three parallel ultralocal models are defined to predict the phase currents of the OW-SynRM within the Cartesian frame. Using the finite-control set technique, the switching states of each H-bridge in the dual inverter are utilized in each ultralocal model to predict the phase currents in the next sampling time. Then, three parallel cost functions decide the optimal switching states. To the authors' knowledge, for the first time, parallel prediction models and cost functions in the Cartesian frame are used in this article for the OW-SynRM. This idea leads to less calculation burden, elimination of the weighting factors, and indirect mitigation of the ZSC in the control process.

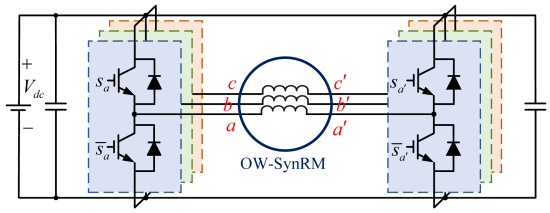

Fig. 1. Configuration of OW-SynRM.

In addition, this article introduces an adaptive proportional-resonant extended state observer (PR-ESO) to improve the estimations required for ultralocal models. The proposed PR-ESO adjusts its estimations based on the motor speed, enabling a variable bandwidth resonant function that adapts to the operating frequency.

In summary, the contributions of this research can be expressed as follows.

1) Applying the MFPCC using parallel cost functions in the ABC frame to achieve up to 73% reductions in the execution time of dual-inverter-fed OWM drives compared to the standard predictive algorithm.
2) Presenting the PR-ESO with adaptive bandwidth based on the motor speed to make the ultralocal model applicable in the ABC frame.
3) Removing the ZSC control loops in the OWM drive by achieving an indirect ZSC regulation.
4) Experimental validation of the proposed MFPCC on the OW-SynRM, which has limited existing literature.
5) Introducing a method capable of application in other multiphase and multilevel applications. Unlike the dq-based technique, the proposed method is much more feasible for multiphase machines.

The rest of this article is organized as follows. Section II models the OW-SynRM and introduces the principles of the dual inverter with a common dc source. The conventional FCS-MPC of the OW-SynRM is discussed in Section III, the details of the proposed method are discussed in Section IV, the experimental results are analyzed in Section V. Finally, Section VI concludes this article.

II. Mathematical Model of the OW-SynRM

The dual-inverter-fed OW-SynRM is schematically shown in Fig. 1, in which a two-level VSI feeds each end of the motor winding, and the dc-links of the VSIs are supplied with a shared source. The output voltage of the dual inverter in the 3-D $\alpha\beta o$

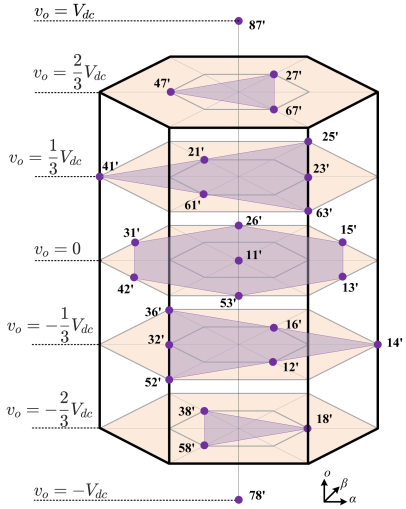

Fig. 2. Space vector locations of the dual inverter with a common DC source.

TABLE I
SWITCHING STATES OF A SINGLE VSI

State	1	2	3	4	5	6	7	8
$s_a s_b s_c$	(100)	(110)	(010)	(011)	(001)	(101)	(000)	(111)

stationary frame is expressed as follows:

$$v_\alpha + jv_\beta = \frac{2}{3}V_{\text{dc}}\left(s_{aa'} + s_{bb'}a + s_{cc'}a^2\right)$$
$$v_o = \frac{1}{3}V_{\text{dc}}\left(s_{aa'} + s_{bb'} + s_{cc'}\right) \tag{1}$$

where V_{dc} is the dc-link voltage, $a = e^{j2\pi/3}$, and $s_{xx'} = s_x - s_{x'}$, $x \in \{a, b, c\}$, and s_x depicting the switching state of the appointed leg. When the upper switch is ON, $s_x = 1$, and when it is OFF, $s_x = 0$. Therefore, the six legs of the dual inverter produce $2^6 = 64$ different switching states leading to 27 unique VVs in the 3-D $\alpha\beta o$ space vector diagram plotted in Fig. 2. The VVs in this figure are labeled according to the state numbers in Table I, and the superscript "′" refers to the second VSI. For example, switching state $23'$ means that the state of the first VSI is (110) and the state of the second VSI is (010).

The literature has noted that utilizing a common dc source for the dual inverter causes ZSC to flow through the motor windings [15]. So, the motor's model should contain the o-axis component. In this regard, the dynamic equation of the OW-SynRM in the rotational reference frame (dqo) is written as follows:

$$\mathbf{L}_{dqo}\frac{\mathrm{d}\mathbf{i}_{dqo}}{\mathrm{d}t} = \mathbf{v}_{dqo} - R_s\mathbf{i}_{dqo} + \omega_e\,\mathbf{j}\boldsymbol{\phi}_{dqo} \tag{2}$$

where $\mathbf{i}_{dqo} = [i_d\, i_q\, i_o]^\intercal$ and $\mathbf{v}_{dqo} = [v_d\, v_q\, v_o]^\intercal$ are the vectors of the current and voltage, respectively. $\boldsymbol{\phi}_{dqo} = [\phi_d\, \phi_q\, 0]^\intercal$ is the flux vector, R_s is the stator resistance, $\mathbf{L}_{dqo} = \text{diag}\{L_d, L_q, L_o\}$ is the dqo inductance matrix, ω_e is the electrical speed, and $\mathbf{j} = \begin{bmatrix} 0 & -1 & 0 \\ 1 & 0 & 0 \\ 0 & 0 & 0 \end{bmatrix}$.

The above model is the key part of the conventional MPC control employed for the OW-SynRM in the next section.

III. APPLYING FCS-MPC FOR OW-SYNRM

In the FCS-MPC, the controlled variables are predicted in the next sampling interval for each possible VV using the discrete dynamic equation of the system. So, the prediction model of the OW-SynRM can be acquired if the model in (2) is discretized by Euler's method, and the VVs of the dual inverter in Fig. 2 are applied to it. The mathematical description is expressed as

$$\mathbf{i}_{dqo}^{k+1}(n) = \mathbf{i}_{dqo}^{k} + t_s\mathbf{L}_{dqo}^{-1}\left(\mathbf{v}_{dqo}(n) - R_s\mathbf{i}_{dqo}^{k} + \omega_e\,\mathbf{j}\boldsymbol{\phi}_{dqo}^{k}\right) \tag{3}$$

where t_s is the sampling time, k denotes the current sample, and $k+1$ refers to the next sample. The term $\mathbf{i}_{dqo}^{k+1}(n)$ depicts the predicted currents for each VV ($\mathbf{v}_{dqo}(n)$) derived from transforming (1) into the dqo coordinates, and $n = 1, \ldots, 27$ denotes the vector number. Among the 27 predicted current components, the one with a minimum error compared to the reference current is selected by a cost function defined as follows:

$$\begin{cases} G(n) = G_{\text{dq}}(n) + W_o G_o(n) \\ G_{\text{dq}}(n) = \left|i_d^* - i_d^{k+1}(n)\right| + \left|i_q^* - i_q^{k+1}(n)\right| \\ G_o(n) = \left|i_o^* - i_o^{k+1}(n)\right| \end{cases} \tag{4}$$

where i_d^* denotes the reference d-axis current, which is set by the flux reference; i_q^* is the reference q-axis current derived from the speed control loop, i_o^* refers to the reference ZSC that should be set to zero to suppress the ZSC, and the parameter W_o is the weighting factor for the zero component. The VV corresponding to the minimum $G(n)$ is directly applied to the dual inverter.

Equations (3) and (4) show that the ZSC has been easily merged into the predictive algorithm owing to the flexibility of the FCS-MPC in controlling multiple variables. However, performing FCS-MPC with 27 VVs demands a high computational burden. Besides, the conventional FCS-MPC strictly depends on the system's model. This can be troublesome in the case of SynRM because L_d and L_q show highly nonlinear behavior due to the direct and cross-magnetization effects [33]. So, the magnetizing curve should be obtained and applied to the model (3).

By scrutinizing these issues, it can be seen that they are fundamentally distinct, thereby requiring unique solutions for each. For the model dependency problem, various studies have been conducted in the literature, such as using robust prediction models [34], disturbance observer-based control [35], model-free predictive control [36], etc. The second issue has been settled using reduced switching candidates [22], cascaded predictive algorithm [28], etc. In [26], a model-free approach has been combined with a cascaded switching algorithm to solve both mentioned issues. Instead of merging various control concepts, the next section presents an MFPCC that inherently has low iterations. So, a reduction of the number of VV candidates is not required.

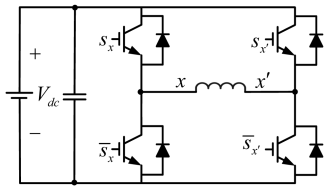

Fig. 3. Full H-bridge inverter feeds each phase of the OW-SynRM.

TABLE II
SWITCHING STATES OF THE PROPOSED METHOD

n	$(s_x s_{x'})$	$s_{xx'}$
1	(10)	1
2	(00) or (11)	0
3	(01)	−1

IV. PROPOSED MFPCC WITH PARALLEL COST FUNCTIONS

A. Conceptualization

This article presents a new predictive control structure for the OW-SynRM based on two concepts.

Concept 1: In the dual inverter, each phase of the OW-SynRM is fed by a full H-bridge inverter as illustrated in Fig. 3. So, it can be considered that each phase has a separate path for the current.

Concept 2: The model-free control theory [37] has a universal dynamic equation expressed in (5), which can be employed in any reference frame as discussed in [32]

$$y^{(n)} = F + bu \tag{5}$$

where u, y, and n are the system's input, output, and degree, respectively. The term F represents all known and unknown dynamics between the input and output and b is the input coefficient that must be tuned.

By manipulating these two concepts, a new MFPCC architecture is presented in Cartesian coordinates. For each H-bridge in the dual inverter, the model-free dynamic equation can be written as follows:

$$\mathrm{d}i_x/\mathrm{d}t = F_x + b(V_{\mathrm{dc}} s_{xx'}) \tag{6}$$

where i_x is the phase current reminding that $x \in \{a, b, c\}$, F_x is an unknown function to be identified, and $s_{xx'}$ is the switching state of the H-bridge according to Table II. The above equation is utilized to construct a parallel prediction algorithm in the following.

B. Parallel Current Predictions and Cost Functions

The discrete format of (6) is employed independently for each phase, and the switching states of Table II are applied to predict the currents in Cartesian coordinates as follows:

$$i_x^{k+1}(n) = i_x^k + t_s F_x + t_s b V_{dc} s_{xx'}(n). \tag{7}$$

In the above equation, n takes $\{1, 2, 3\}$ because $s_{xx'}$ only has three different states as shown in Table II. This means the predictive algorithm is significantly simplified compared to the standard algorithm with 27 VVs. In other words, there are three predicted current values for each phase. The optimum current value of each phase is chosen among these values using a separate cost function. Therefore, three parallel cost functions are employed in the proposed methodology as follows:

$$\begin{cases} G_x(n) = \left| i_x^* - i_x^{k+1}(n) \right| \\ x = a, b, c \\ n = 1, 2, 3 \end{cases} \tag{8}$$

where i_x^* depicts the reference current value of phase x, and it can be attained by transforming the dq current references (i_d^* and i_q^*) to the Cartesian frame as follows:

$$i_x^* = i_d^* \sin\left(\theta - \frac{2\pi(j-1)}{3}\right) + i_q^* \cos\left(\theta - \frac{2\pi(j-1)}{3}\right) \tag{9}$$

note that $j = 1$ for phase a, $j = 2$ for phase b, and $j = 3$ for phase c.

Notably, the q-axis current reference is derived from the speed control loop, which is implemented using a conventional PI controller in this study as

$$i_q^* = \left(k_P + \frac{k_I}{s}\right)(\omega^* - \omega_e) \tag{10}$$

where ω^* is the speed reference; k_P and k_I are the coefficients of the PI controller. In SynRMs, the d-axis current reference is typically determined using the maximum torque per ampere technique, where $i_d^* = i_q^*$. However, since optimization is not the focus of this study, a constant value is assigned to i_d^* in the experiments to simplify the implementation.

The proposed MFPCC can be applied with the finite control-set algorithm using (7)–(9) knowing that F_x is estimated with a proper observer in the following section.

C. Introducing PR-ESO to Estimate Unknown F_x

In the literature, various types of ESOs have been utilized to estimate F_x either in the synchronous or the stationary reference frames [38], [39]. This article presents a modified ESO in the Cartesian coordinates. It is worth noting that the motor currents have a variable frequency depending on the synchronous speed. Therefore, to ensure that the proposed MFPCC performs effectively in different operating points, an adaptive PR-ESO is presented here as follows:

$$\begin{cases} \mathrm{d}\hat{i}_x/\mathrm{d}t = \hat{F}_x + bV_{dc} s_{xx'} + \beta_1 e_x \\ \mathrm{d}\hat{F}_x/\mathrm{d}t = k_P e_x + E_R(e_x) \end{cases} \tag{11}$$

where the superscript "$\hat{}$" determines the estimated variables, $e_x = i_x - \hat{i}_x$, β_1 is the observer gain, k_P is the proportional coefficient, and $E_R(e_x)$ is a resonant error function with the following frequency-domain system:

$$E_R(s) = \frac{k_R \omega_e s}{s^2 + k_R \omega_e s + w_e^2} e_x \tag{12}$$

where ω_e represents the bandwidth of the resonant observer and k_R is the resonant gain. In the proposed PR-ESO, the bandwidth is set equal to the motor's electrical speed. Therefore,

the proposed MFPCC adapts to the speed of the OW-SynRM and ensures precise control at different operating points. The time-domain system of the proposed observer can be rewritten as follows:

$$\begin{cases} \mathrm{d}\hat{i}_x/\mathrm{d}t = \hat{F}_x + bV_{\mathrm{dc}}s_{xx'} + \beta_1 e_x \\ \mathrm{d}E_R/\mathrm{d}t = k_R\omega_e e_x - k_R\omega_e E_R - \omega_e^2 \int E_R \mathrm{d}t \\ \mathrm{d}\hat{F}_x/\mathrm{d}t = k_P e_x + E_R \end{cases}. \tag{13}$$

To analyze the stability of the above system, the state-space model is defined by choosing four state variables: $x_1 = \hat{i}_x$, $x_2 = E_R$, $x_3 = \int E_R \mathrm{d}t$, and $x_4 = \hat{F}_x$. The inputs of the observer are the measured current and the switching state of phase x, i.e., $u_1 = i_x$ and $u_2 = s_{xx'}$. The state-space system is expressed as follows:

$$\begin{bmatrix} \dot{x}_1 \\ \dot{x}_2 \\ \dot{x}_3 \\ \dot{x}_4 \end{bmatrix} = \begin{bmatrix} -\beta_1 & 0 & 0 & 1 \\ -k_R\omega_e & -k_R\omega_e & -\omega_e^2 & 0 \\ 0 & 1 & 0 & 0 \\ -k_P & 1 & 0 & 0 \end{bmatrix} \begin{bmatrix} x_1 \\ x_2 \\ x_3 \\ x_4 \end{bmatrix} + \begin{bmatrix} \beta_1 & bV_{dc} \\ k_R\omega_e & 0 \\ 0 & 0 \\ k_P & 0 \end{bmatrix} \begin{bmatrix} u_1 \\ u_2 \end{bmatrix}. \tag{14}$$

Considering the general state-space system $\dot{\mathbf{x}} = \mathbf{A}\mathbf{x} + \mathbf{B}\mathbf{u}$, the coefficient matrix $\mathbf{A}$ for the above system is

$$\mathbf{A} = \begin{bmatrix} -\beta_1 & 0 & 0 & 1 \\ -k_R\omega_e & -k_R\omega_e & -\omega_e^2 & 0 \\ 0 & 1 & 0 & 0 \\ -k_P & 1 & 0 & 0 \end{bmatrix}. \tag{15}$$

The characteristic polynomial is obtained by

$$P(s) = \det(s\mathbf{I} - \mathbf{A}) \tag{16}$$

where $\mathbf{I}$ is the identity matrix. Therefore

$$P(s) = s^4 + a_3 s^3 + a_2 s^2 + a_1 s + a_0.$$

$$\begin{cases} a_0 &= k_R\omega_e^2 \\ a_1 &= \beta_1\omega_e^2 + k_R\omega_e + k_P k_R\omega_e \\ a_2 &= \beta_1 k_R\omega_e + \omega_e^2 + k_R \\ a_3 &= \beta_1 + k_R\omega_e. \end{cases} \tag{17}$$

Based on the Routh–Hurwitz stability criterion, to ensure the stability of the system, all the coefficients of $P(s)$ must be positive ($a_i > 0$) and satisfy $a_3a_2a_1 > a_1^2 + a_3^2a_0$.

D. Digital Implementation Process of the Proposed MFPCC

Fig. 4 illustrates the block diagram of the proposed method. Initially, the measured three-phase currents are directly utilized in the proposed PR-ESO to estimate the unknown functions ($\hat{F}_x$). It is worth noting that in conventional methods, measured currents are transformed into orthogonal reference frames. This stage is removed in the proposed method. The PR-ESO given in

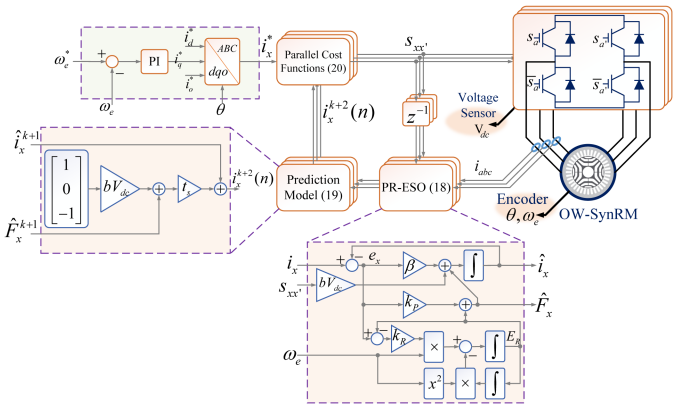

Fig. 4. Block diagram of the proposed MFPCC with parallel cost functions.

(11) is expressed in the discrete domain as follows:

$$\begin{cases} \hat{i}_x^{k+1} = \hat{i}_x^k + t_s\left(\hat{F}_x^k + bV_{dc}s_{xx'}^k + \beta_1 e_x^k\right) \\ E_R^{k+1} = E_R^k + t_s\left(k_R\omega_e e_x^k - k_R\omega_e E_R^k - \omega_e^2 H_R^k\right) \\ H_R^{k+1} = H_R^k + t_s\left(E_R^k\right) \\ \hat{F}_x^{k+1} = \hat{F}_x^k + t_s\left(k_P e_x^k + E_R^k\right) \end{cases} \tag{18}$$

where H_R is an intermediate function used to model the integral action in the discrete domain.

Second, the estimated variables are put into the prediction models to obtain the currents in the future sampling interval. In this stage, each phase current is predicted for three possible switching states given in Table II. To compensate for the digital implementation delay, the predictions are made for the instant $(k+2)$ using the estimations from the instant $(k+1)$ based on (18) as follows:

$$i_x^{k+2}(n) = \hat{i}_x^{k+1} + t_s\hat{F}_x^{k+1} + t_s bV_{dc}s_{xx'}^{k+1}(n). \tag{19}$$

For a precise current prediction, a voltage sensor for the dc-link voltage V_{dc} is recommended, especially in the drive system that utilizes a rectified dc source. Finally, the parallel cost functions determine the optimal switching state for each phase, taking into account the reference current values obtained in (9). The proposed cost function in the digital implementation is defined as follows:

$$\begin{cases} G_x(n) = \left|i_x^* - i_x^{k+2}(n)\right|^2 \\ x = a, b, c \\ n = 1, 2, 3. \end{cases} \tag{20}$$

E. Remarks on the Proposed MFPCC Compared to MFPCCs in Orthogonal Coordinates

The MFPCC in the Cartesian frame offers several significant advantages over conventional MFPCCs that operate in orthogonal coordinate systems, such as the dqo or $\alpha\beta o$ frames. These benefits are particularly evident when comparing the flowchart of the proposed method [see Fig. 5(b)] to that of the standard predictive control methods [see Fig. 5(a)].

1) *Reduced Computational Burden:* One of the key advantages of the proposed methodology is its reduced computational burden. In the conventional method, the predictive algorithm must be repeated 27 times for three orthogonal

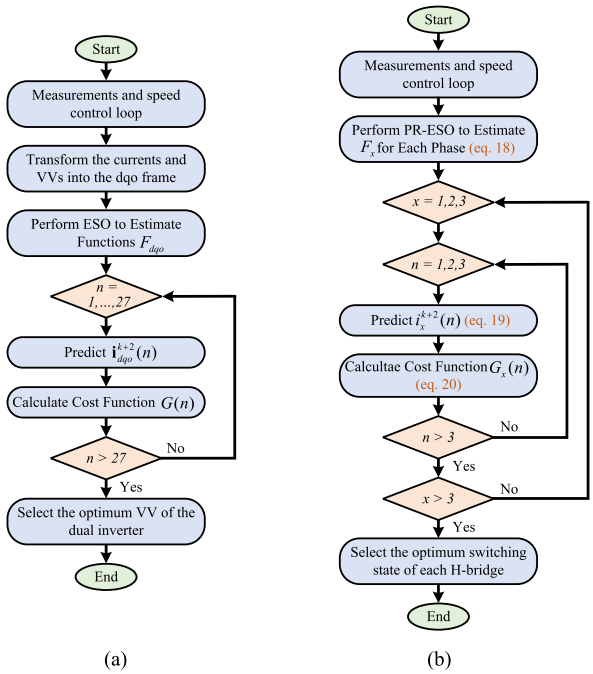

Fig. 5. Flowcharts of the MFPCC algorithm. (a) Standard approach in the orthogonal coordinates. (b) Proposed approach in the Cartesian coordinates.

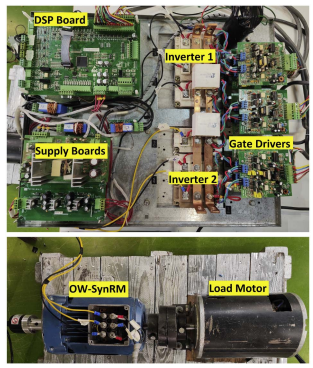

Fig. 6. Experimental setup.

TABLE III
SYNRM SPECIFICATIONS

Name	Symbol	Value
Rated line voltage	V_{L-L}	400 v
Rated torque	T_e	3.1 N.m
Rated speed	N	1500 r/min
Pola pairs	P	2
Stator resistance	R_s	9.1 Ω
d-axis inductance	L_d	0.22 H
q-axis inductance	L_q	0.04 H
o-axis inductance	L_0	0.03 H

current components (dqo), whereas the proposed algorithm only requires 3 repetitions for three phase currents (ABC). This means 89% reduction in algorithm repetition. Moreover, there is no need for the lookup tables to store 27 voltage vectors. These features are beneficial for low-cost microprocessors.

2) *Direct Phase Current Regulation:* The proposed MFPCC directly regulates each phase current and eliminates the ZSC control loop. In contrast, conventional methods utilize additional control loops, such as the hysteresis controller to manage the ZSC. Therefore, the proposed method has a simpler structure in this regard. This direct regulation is not only effective for the OWM drives but also extends to other advanced systems, such as unbalanced grids using four-leg inverters, fault-tolerant controls, and multilevel multiphase inverters.
3) *Flexibility of the control algorithm:* The proposed method offers significant flexibility because it can be easily adapted for different types of dual inverters with common or isolated dc sources. The reason is that the proposed method in the ABC frame does not require a space vector diagram, while the conventional MFPCC in the orthogonal frame requires the specific space vector diagram of the utilized inverter.
4) *Elimination of Weighting Factors:* The cost function in the orthogonal frame (4) needs a weighting factor W_o for the ZSC term. However, the proposed method utilizes separate cost functions that do not require any weighting factors.
5) *Minimized Frame Transformations:* The proposed method also reduces the number of frame transformations. While the MFPCC in the dqo rotary frame requires the transformation of both measured currents and VVs, the proposed approach only requires the transformation of reference currents. This reduction in frame transformations simplifies the control process and improves computational efficiency.

While the proposed method offers several advantages, a few limitations should be considered. First, it is primarily designed to simplify the predictive algorithm for complex inverters, so applying it in the Cartesian frame for standard two-level three-phase inverters may be more than necessary. Second, because the algorithm operates in the Cartesian frame, it does not directly use SVPWM if a continuous control-set scheme is applied. However, the SVPWM can be applied by transforming the voltage references into the stationary frame. Despite these considerations, the advantages of the proposed method, particularly in reducing computational burden and increasing flexibility, make it a useful approach for complicated systems.

V. EXPERIMENTAL RESULTS

An experimental setup of the dual-inverter-fed OW-SynRM has been developed to test and validate the proposed MFPCC. Fig. 6 illustrates the setup, and Table III provides the specification of the OW-SynRM. The TMS320F28335 DSP microprocessor is employed to implement the control system with a 50 -μs sampling time.

In this experimental setup, the rotor position is measured by a typical incremental encoder. It should be noted that accurate determination of the initial rotor position is crucial for the successful startup of SynRM drives, regardless of whether encoders are

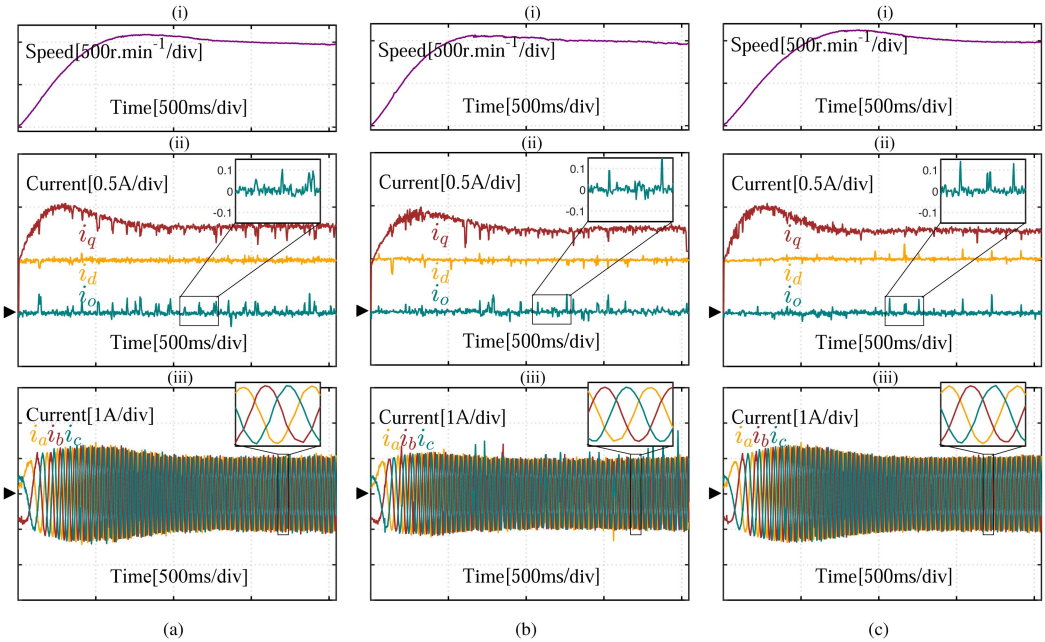

Fig. 7. Dynamic response of the dual-inverter-fed OW-SynRM at startup with speed reference 1000 r/min. (a) MFPCC-dqo. (b) MFPCC-$\alpha\beta$. (c) MFPCC-ABC. The waveforms are (i) motor speed, (ii) dqo current components, and (iii) three-phase currents.

employed [6], [40], [41]. Failure to do so can lead to issues, such as sudden jitter, brief reversals, or startup failure. In addition, the control system requires precise initial position information to ensure maximum starting torque. Since the incremental encoder cannot provide the initial position of the rotor, an initial position estimation method was used in the control method [6]. Before the main control method begins, this estimation method calculates the initial position of the OW-SynRM.

In this section, various test scenarios are conducted to analyze the performance of the proposed control system in the Cartesian frame compared to existing control schemes in the stationary frame and the dq rotational frame. The control methods under consideration are listed as follows.

1) *MFPCC-dqo:* A conventional finite control-set approach, applying all 27 VVs to the ultralocal model in the dq rotational frame [25], [42].
2) *MFPCC-$\alpha\beta o$:* A sequential finite control-set approach, applying 7 VVs for each inverter (14 iterations) in the $\alpha\beta$ stationary frame [26].
3) *MFPCC-ABC:* Proposed finite control-set approach, applying three voltages for each phase (nine iterations) in the Cartesian frame.

A. Dynamic Response

The three mentioned MFPCC approaches are tested under dynamic conditions using the experimental setup. The first dynamic test involves the motor startup from the standstill to 1000 r/min. Fig. 7 presents the results of this test. As shown, the proposed MFPCC-ABC exhibits a dynamic response comparable to the other two methods, but with slightly lower current distortion and ZSC levels. The higher distortion in the MFPCC-dqo method is due to its higher computational burden, which necessitates a longer sampling time—twice that of the other two methods. In addition, the MFPCC-$\alpha\beta o$ method displays higher distortion due to its sequential algorithm with fewer VVs. This test confirms that the MFPCC-ABC approach maintains a strong dynamic response while simplifying the prediction algorithm. It is worth noting that the similar dynamic responses of the three control methods can be attributed to their use of the same speed control loop. However, the MFPCC-$\alpha\beta o$ method has a slower dynamic response due to its sequential algorithm, which prioritizes the ZSC suppression over the control of the torque-producing current component (i_q). The second dynamic test evaluates the performance of the three MFPCC approaches under a sudden load application. In this scenario, the OW-SynRM was operating under no-load conditions at 750 r/min when the load was abruptly applied. The results of this test are presented in Fig. 8. The dynamic responses of all three methods were found to be similar by effectively recovering the motor to its normal operation; however, the MFPCC-$\alpha\beta o$ method exhibited slower dynamic and higher current distortion compared to the other approaches. This increased distortion is attributed to the method's sequential algorithm with fewer VVs. Meanwhile, the MFPCC-dqo method demonstrated a slightly higher ripple in dq currents due to its longer sampling time due to the higher computational load. In contrast, the proposed MFPCC-ABC approach delivered superior performance, with lower distortion and ripple, while maintaining a strong dynamic response. In addition, the fact that ZSC suppression remained consistent during the transient period verifies the effectiveness of the proposed method in indirectly controlling the ZSC. This test further confirms the effectiveness of the MFPCC-ABC method in managing dynamic conditions with improved overall performance.

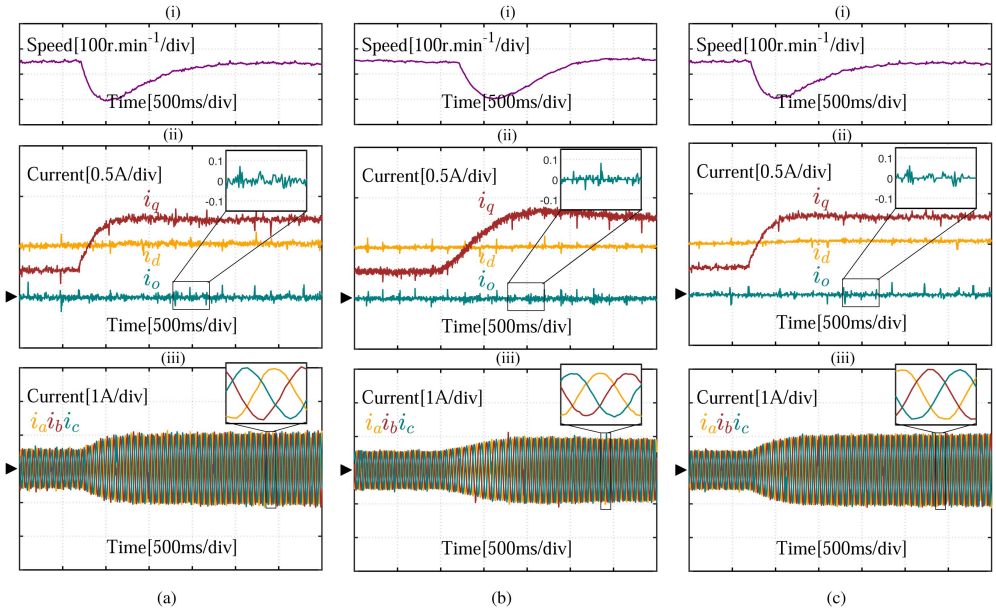

Fig. 8. Dynamic response of the dual-inverter-fed OW-SynRM when the load is suddenly applied. (a) MFPCC-dqo. (b) MFPCC-$\alpha\beta$. (c) MFPCC-ABC. The waveforms are (i) motor speed, (ii) dqo current components, and (iii) three-phase currents.

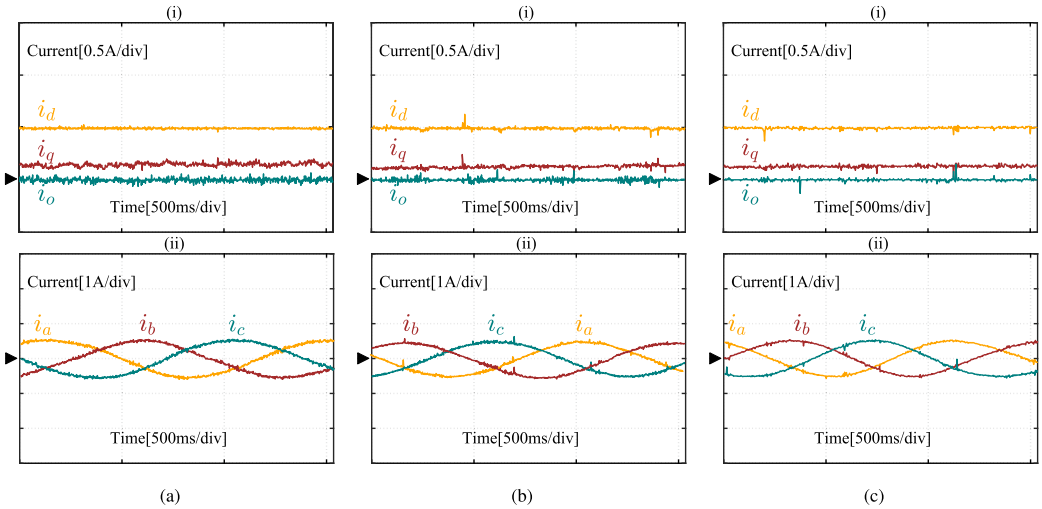

Fig. 9. Steady-state responses of the three MFPCC approaches at a very low speed of 20 r/min under a light load. (a) MFPCC-dqo. (b) MFPCC-$\alpha\beta o$. (c) MFPCC-ABC. Waveforms are (i) dqo current components and (ii) three-phase currents.

B. Steady-State Response

The steady-state performance of the three MFPCC approaches was evaluated at two different operating speeds: 20 and 1000 r/min, with the load provided by a dc machine. It is important to note that the higher speed test at 1000 r/min corresponds to a higher load condition. The results are summarized in Figs. 9 and 10.

At 20 r/min, each method's total harmonic distortion (THD) values were as follows: MFPCC-dqo: 8.2%, MFPCC-$\alpha\beta o$: 6.88%, and the proposed MFPCC-ABC: 6.67%. As these results indicate, the proposed MFPCC-ABC method exhibited the lowest THD, demonstrating its superior ability to minimize harmonic distortion at low speeds. The current components in the dqo frame also showed that the MFPCC-ABC method provided better suppression of the ZSC compared to the other two methods.

At 1000 r/min, the THD results further highlighted the advantages of the proposed method. The THD values were as follows: MFPCC-dqo: 5.26%, MFPCC-$\alpha\beta o$: 5.41%, and MFPCC-ABC: 3.64%. The significantly lower THD in the MFPCC-ABC method at high speed compared to the other techniques can be attributed to two main factors. First, its simple algorithm with reduced computational complexity, achieved by applying parallel cost functions, allows for implementation with a shorter sampling time. This gives the MFPCC-ABC method an advantage over the MFPCC-dqo, which relies on a more computationally intensive algorithm. Second, the proposed PR-ESO enhances

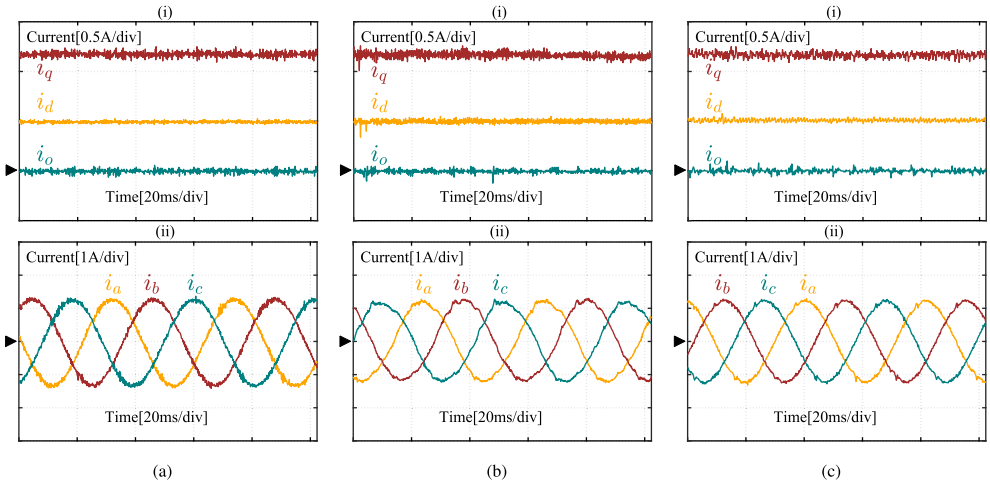

Fig. 10. Steady-state responses of the three MFPCC approaches at the speed of 1000 r/min under load. (a) MFPCC-dqo. (b) MFPCC-$\alpha\beta o$. (c) MFPCC-ABC. Waveforms are (i) dqo current components and (ii) three-phase currents.

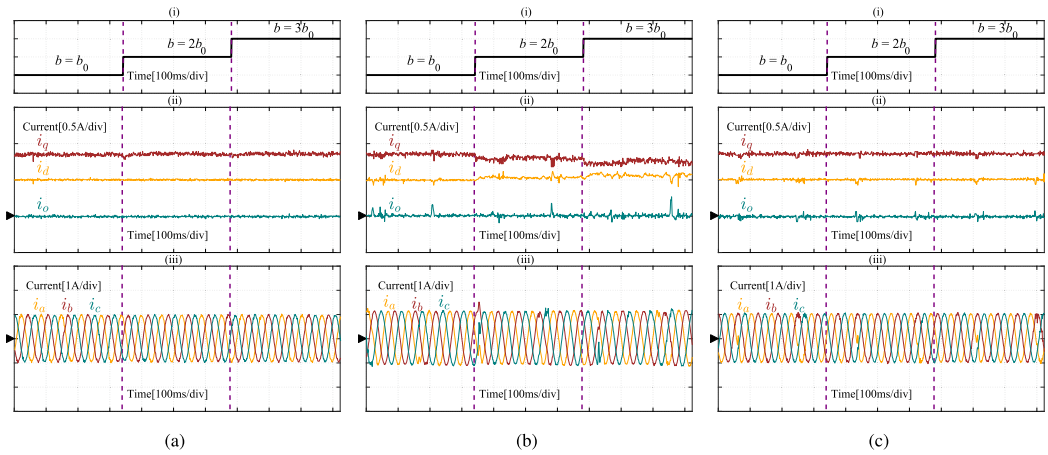

Fig. 11. Effect of the input coefficient variation on the performance of the MFPCC methods. (a) MFPCC-dqo. (b) MFPCC-$\alpha\beta o$. (c) MFPCC-ABC. Waveforms are (i) value of b, (ii) dqo current components, and (iii) three-phase currents.

the current tracking performance of the MFPCC-ABC method compared to the MFPCC-$\alpha\beta o$ method. The traditional ESO used in the MFPCC-$\alpha\beta o$ method faces convergence issues at higher speeds, negatively impacting its performance.

These steady-state tests confirm that the MFPCC-ABC method outperforms the MFPCC-dqo and MFPCC-$\alpha\beta o$ approaches, offering lower THD and better control of the ZSC across different speeds.

C. Effect of the Local Parameter Variation

The MFPCC methods are inherently model-free and thus, do not depend on the OW-SynRM parameters. However, the design of the local parameters in a model-free approach can still be influenced by the motor parameters [26], [43]. To assess this effect, a test scenario was conducted where the input coefficient b was varied by 100% and 200% in two steps from its initial value b_0. The results for the three MFPCC methods are compared in Fig. 11.

The results reveal that a 200% change in b does not significantly deteriorate the performance of the MFPCC-dqo. In contrast, the MFPCC-$\alpha\beta o$ method exhibits poor performance with changes in the coefficient b. This poor performance can be attributed to two factors: the use of a reduced number of VVs in the sequential algorithm and the reliance on a traditional ESO for sinusoidal variables in the $\alpha\beta$ stationary frame, which makes the design more sensitive. On the other hand, the proposed MFPCC-ABC method, utilizing parallel cost functions and a modified PR-ESO, achieves robustness comparable to that of the MFPCC-dqo while significantly reducing algorithm iterations, leading to a computationally effective algorithm.

D. Comparative Analysis of the MFPCC Methods

Table IV provides a comparative overview of the three MFPCC methods as follows: MFPCC-dqo, MFPCC-$\alpha\beta o$, and the proposed MFPCC-ABC. The comparison is based on several key performance metrics, including THD at high speed, ZSC levels,

TABLE IV
COMPARISON OF THE RESULTS

Method	ZSC level (A)	THD i_a	WF	iterations	Calc. time (μs)
MFPCC-dqo	< 0.05	5.26%	yes	27	72.3
MFPCC-$\alpha\beta o$	< 0.05	5.41%	yes	14	21.4
Proposed Method	< 0.05	3.64%	no	9	18.7

the need for a weighting factor in the cost function, algorithm iterations, and execution time on the microprocessor.

As previously discussed, the proposed MFPCC-ABC method achieves the lowest THD at high speed. It is also noteworthy that all three methods maintain ZSC levels close to zero, demonstrating effective ZSC suppression across the board. Notably, the MFPCC-ABC method achieves this ZSC suppression without requiring direct ZSC control, highlighting the merit of the proposed parallel cost functions. A key advantage of the MFPCC-ABC method is that it does not require a weighting factor in the cost function, simplifying the design process. In contrast, both MFPCC-dqo and MFPCC-$\alpha\beta o$ require a weighting factor to balance the tradeoffs in their respective cost functions.

In terms of algorithm efficiency, the MFPCC-ABC method also stands out with only 9 iterations, compared to 27 for MFPCC-dqo and 14 for MFPCC-$\alpha\beta o$. Note that MFPCC-$\alpha\beta o$ [26] has proposed a successful computational reduction technique. However, this reduction slightly deteriorated the current quality. The proposed MFPCC-ABC method achieves an execution time of 18.7 μs, significantly lower than the 71.1 μs for MFPCC-dqo and 21.4 μs for MFPCC-$\alpha\beta o$ without deteriorating the current compared to the 27 vector method.

Overall, the MFPCC-ABC method offers superior performance, computational efficiency, and simplicity, making it a highly effective approach compared to the other two methods.

VI. CONCLUSION

This article has proposed a novel MFPCC approach that integrates parallel current predictions and cost functions in the Cartesian frame for OW-SynRM drives. Through rigorous comparative experimental tests, it has been confirmed that the proposed MFPCC algorithm significantly reduces computational burden while maintaining the high performance of standard implementations. Specifically, the execution time is reduced by 73% compared to the MFPCC-dqo and by 13% compared to the sequential MFPCC-$\alpha\beta o$. In addition, the THD is decreased by 1.6% compared to the conventional MFPCC-dqo and by 1.8% compared to the MFPCC-$\alpha\beta o$.

Furthermore, the proposed approach effectively mitigates ZSC, achieving suppression indirectly, comparable to methods that rely on direct ZSC control. In light of these achievements, it can be concluded that the MFPCC with parallel cost functions in the Cartesian frame represents an effective and efficient control alternative for open-end winding motor drives. Moreover, the versatility of the proposed method suggests its potential applicability in a variety of other complex power electronic systems, such as four-leg inverters for unbalanced grids, fault-tolerant control systems, and multilevel and multiphase inverters. Future research could extend the benefits of the proposed MFPCC with parallel cost functions to a broader range of advanced inverter systems.

REFERENCES

[1] Y. Zuo, X. Zhu, X. Si, and C. H. T. Lee, "Fault-tolerant control for multiple open-leg faults in open-end winding permanent magnet synchronous motor system based on winding reconnection," *IEEE Trans. Power Electron.*, vol. 36, no. 5, pp. 6068–6078, May 2021.

[2] L. Xu and Z. Q. Zhu, "A novel SVPWM for open winding permanent magnet synchronous machine with extended operation range," *IEEE Trans. Emerg. Sel. Topics Power Electron.*, vol. 11, no. 1, pp. 901–914, Feb. 2023.

[3] U. R. Muduli, A. R. Beig, R. K. Behera, K. A. Jaafari, and J. Y. Alsawalhi, "Predictive control with battery power sharing scheme for dual open-end-winding induction motor based four-wheel drive electric vehicle," *IEEE Trans. Ind. Electron.*, vol. 69, no. 6, pp. 5557–5568, Jun. 2022.

[4] H. Matsumori, Y. Maeda, T. Kosaka, N. Matsui, and S. Saha, "Dual inverter-fed open winding IPMSM drive system for high-power premium class EV," *IEEE Trans. Ind. Appl.*, vol. 59, no. 2, pp. 2069–2080, Mar./Apr. 2023.

[5] A. Credo, I. Petrov, J. Pyrhönen, and M. Villani, "Impact of manufacturing stresses on multiple-rib synchronous reluctance motor performance," *IEEE Trans. Ind. Appl.*, vol. 59, no. 2, pp. 1253–1262, Mar./Apr. 2023.

[6] H. Pairo, B. Nikmaram, and S. Mohamadian, "Adaptive-based accurate rotor initial position estimation in synchronous reluctance motors," *IEEE Trans. Ind. Electron.*, vol. 71, no. 11, pp. 13812–13821, Nov. 2024.

[7] G. Du, G. Zhang, H. Li, and C. Hu, "Comprehensive comparative study on permanent-magnet-assisted synchronous reluctance motors and other types of motor," *Appl. Sci.*, vol. 13, no. 14, 2023, Art. no. 8557 .

[8] M. Murataliyev, M. Degano, M. Di Nardo, N. Bianchi, and C. Gerada, "Synchronous reluctance machines: A comprehensive review and technology comparison," *Proc. IEEE*, vol. 110, no. 3, pp. 382–399, Mar. 2022.

[9] C. Zhang, C. Gan, K. Ni, Z. Yu, H. Shi, and R. Qu, "Phase current reconstruction of open-winding synchronous reluctance motor based on edge-alignment and phase-shift strategy," *IEEE Trans. Power Electron.*, vol. 37, no. 5, pp. 5173–5185, May 2022.

[10] J. Riccio, L. Rovere, S. Odhano, M. Di Nardo, and P. Zanchetta, "Model-predictive control of open-end winding synchronous reluctance motor drives," in *Proc. IEEE Energy Convers. Congr. Expo.*, 2022, pp. 1–8.

[11] M. Mengoni, A. Amerise, G. Rizzoli, L. Zarri, A. Tani, and D. Casadei, "Control system for open-end winding sync-rel motors with a floating capacitor bridge," in *Proc. 44th Annu. Conf. IEEE Ind. Electron. Soc.*, 2018, pp. 5695–5701.

[12] W. Hu, C. Ruan, H. Nian, and D. Sun, "An improved modulation technique with minimum switching actions within one PWM cycle for open-end winding PMSM system with isolated DC bus," *IEEE Trans. Ind. Electron.*, vol. 67, no. 5, pp. 4259–4264, May 2020.

[13] W. Hu, C. Ruan, H. Nian, and D. Sun, "Simplified modulation scheme for open-end winding PMSM system with common DC bus under open-phase fault based on circulating current suppression," *IEEE Trans. Power Electron.*, vol. 35, no. 1, pp. 10–14, Jan. 2020.

[14] L. Rovere, G. Valente, A. Formentini, and P. Zanchetta, "Parameters and volt–ampere ratings of a floating capacitor open-end winding synchronous motor drive for extended CPSR," *IEEE Trans. Ind. Electron.*, vol. 69, no. 5, pp. 4576–4586, May 2022.

[15] A. Somani, R. K. Gupta, K. K. Mohapatra, and N. Mohan, "On the causes of circulating currents in PWM drives with open-end winding AC machines," *IEEE Trans. Ind. Electron.*, vol. 60, no. 9, pp. 3670–3678, Sep. 2013.

[16] Z. Dong, Z. Song, W. Wang, and C. Liu, "Improved zero-sequence current hysteresis control-based space vector modulation for open-end winding PMSM drives with common DC bus," *IEEE Trans. Ind. Electron.*, vol. 70, no. 10, pp. 10755–10760, Oct. 2023.

[17] L. Cheng, H. Jianhui, and S. Jing, "Dual-vector predictive current control of open-end winding PMSM with zero-sequence current hysteresis control," *IEEE Trans. Emerg. Sel. Topics Power Electron.*, vol. 10, no. 1, pp. 184–195, Feb. 2022.

[18] W. Hu, C. Ruan, H. Nian, and D. Sun, "Zero-sequence current suppression strategy with common-mode voltage control for open-end winding PMSM drives with common DC bus," *IEEE Trans. Ind. Electron.*, vol. 68, no. 6, pp. 4691–4702, Jun. 2021.

[19] L. Zhong and S. Hu, "Zero-sequence-current suppression of open-end winding PMSM with common DC bus based on virtual vector control," *IEEE Trans. Ind. Electron.*, vol. 71, no. 3, pp. 2356–2364, Mar. 2024.
[20] X. Zhang, W. Zhang, C. Xu, Y. Li, Y. Wang, and D. Gao, "3-D vector-based model predictive current control for open-end winding PMSG system with zero-sequence current suppression," *IEEE Trans. Emerg. Sel. Topics Power Electron.*, vol. 9, no. 1, pp. 242–258, Feb. 2021.
[21] X. Lin, W. Huang, W. Jiang, Y. Zhao, X. Wu, and S. Zhu, "Predictive torque control for open-end winding PMSM with common dc bus based on weighting factorless and finite control set optimization," *IEEE Trans. Emerg. Sel. Topics Power Electron.*, vol. 9, no. 2, pp. 1479–1493, Apr. 2021.
[22] S. G. Petkar and V. K. Thippiripati, "A simplified predictive current control of open-end winding permanent magnet synchronous motor," *IEEE Trans. Power Electron.*, vol. 38, no. 1, pp. 816–826, Jan. 2023.
[23] R. E. Kodumur Meesala, V. P. K. Kunisetti, and V. Kumar Thippiripati, "Enhanced predictive torque control for open end winding induction motor drive without weighting factor assignment," *IEEE Trans. Power Electron.*, vol. 34, no. 1, pp. 503–513, Jan. 2019.
[24] K. V. Praveen Kumar and T. Vinay Kumar, "Predictive torque control of open-end winding induction motor drive fed with multilevel inversion using two two-level inverters," *IET Electric Power Appl.*, vol. 12, no. 1, pp. 54–62, 2018.
[25] M. S. Mousavi, S. A. Davari, B. Nikmaram, A. Nassaji, F. Flores-Bahamonde, and J. Rodríguez, "Reducing calculation time in finite-set model predictive control of open-end winding synchronous reluctance motors," in *Proc. IEEE 18th Int. Conf. Compat., Power Electron. Power Eng.*, 2024, pp. 1–6.
[26] M. S. Mousavi, S. A. Davari, V. Nekoukar, C. Garcia, and J. Rodriguez, "Computationally efficient model-free predictive control of zero-sequence current in dual inverter fed induction motor," *IEEE Trans. Emerg. Sel. Topics Power Electron.*, vol. 11, no. 2, pp. 1332–1344, Apr. 2023.
[27] X. Zhang, H. Zhang, and K. Yan, "Hybrid vector model predictive control for open-winding PMSM drives," *IEEE Trans. Transport. Electrific.*, vol. 10, no. 2, pp. 4322–4333, Jun. 2024.
[28] C. Zhang, C. Gan, K. Ni, Z. Yu, S. Wang, and R. Qu, "Computationally efficient cascaded predictive control for hybrid-inverter fed open-winding PMSM drive with fast partial preselection," *IEEE Trans. Power Electron.*, vol. 39, no. 3, pp. 3509–3520, Mar. 2024.
[29] Y. Wei, H. Young, D. Ke, D. Huang, F. Wang, and J. Rodríguez, "Adaptive ultra-localized time-series for improved model-free predictive current control on PMSM drives," *IEEE Trans. Power Electron.*, vol. 39, no. 5, pp. 5155–5165, May 2024.
[30] B. Long, J. Zhang, D. Shen, J. Rodríguez, J. M. Guerrero, and K. t. Chong, "Ultralocal model-free predictive control of T-type grid-connected converters based on extended sliding-mode disturbance observer," *IEEE Trans. Power Electron.*, vol. 38, no. 12, pp. 15494–15508, Dec. 2023.
[31] S. A. Davari, S. Azadi, F. Flores-Bahamonde, F. Wang, P. Wheeler, and J. Rodriguez, "Compensating the measurement error in model-free predictive control of induction motor via kalman filter-based ultra-local model," *IEEE Trans. Power Electron.*, vol. 39, no. 12, pp. 15811–15821, Dec. 2024.
[32] M. S. Mousavi, S. Alireza Davari, F. Flores, C. Garcia, and J. Rodriguez, "Abc frame model-free predictive control for multiphase converters and electrical drives," in *Proc. IEEE Int. Conf. Predictive Control Elect. Drives Power Electron.*, 2023, pp. 1–6.
[33] J. Riccio, P. Karamanakos, S. Odhano, M. Tang, M. Dim Nardo, and P. Zanchetta, "Direct model predictive control of synchronous reluctance motor drives," *IEEE Trans. Ind. Appl.*, vol. 59, no. 1, pp. 1054–1063, Jan./Feb. 2023.
[34] I. Oliani, R. Figueiredo, L. F. N. Lourenço, A. Pelizari, and A. J. S. Filho, "Robust predictive current control using discrete-time integral action for induction motors," *IEEE Trans. Emerg. Sel. Topics Power Electron.*, vol. 11, no. 6, pp. 5766–5773, Dec. 2023.
[35] C. Sheng, Q. Wang, T. Su, and H. Wang, "Induction motor torque closed-loop vector control system based on flux observation and harmonic current suppression," *Control Eng. Pract.*, vol. 142, 2024, Art. no. 105755. [Online]. Available: https://www.sciencedirect.com/science/article/pii/S0967066123003246
[36] Y. Wei, D. Ke, F. Wang, and M. L. Heldwein, "Model-free predictive sliding mode control for PMSM drives using ultra-local method," in *Proc. 49th Annu. Conf. IEEE Ind. Electron. Soc.*, 2023, pp. 1–6.
[37] M. Fliess and C. Join, "Model-free control," *Int. J. Control*, vol. 86, no. 12, pp. 2228–2252, 2013.
[38] Y. Wei, H. Young, D. Ke, F. Wang, and J. Rodríguez, "Model-free predictive current control using extended affine ultralocal for pmsm drives," *IEEE Trans. Ind. Electron.*, vol. 71, no. 7, pp. 6719–6729, Jul. 2024.
[39] M. S. Mousavi, S. A. Davari, V. Nekoukar, C. Garcia, and J. Rodriguez, "Integral sliding mode observer-based ultralocal model for finite-set model predictive current control of induction motor," *IEEE Trans. Emerg. Sel. Topics Power Electron.*, vol. 10, no. 3, pp. 2912–2922, Jun. 2022.
[40] E. Daryabeigi, H. A. Zarchi, G. A. Markadeh, J. Soltani, and F. Blaabjerg, "Online MTPA control approach for synchronous reluctance motor drives based on emotional controller," *IEEE Trans. Power Electron.*, vol. 30, no. 4, pp. 2157–2166, Apr. 2015.
[41] F.-J. Lin, M.-S. Huang, S.-G. Chen, C.-W. Hsu, and C.-H. Liang, "Adaptive backstepping control for synchronous reluctance motor based on intelligent current angle control," *IEEE Trans. Power Electron.*, vol. 35, no. 7, pp. 7465–7479, Jul. 2020.
[42] X. Li, S. Zhang, C. Zhang, Y. Zhou, X. Yuan, and S. Wang, "A novel zero sequence current suppression scheme for open-winding permanent magnet synchronous motor based on model-free control," *IEEE Trans. Ind. Electron.*, vol. 71, no. 8, pp. 8560–8570, Aug. 2024.
[43] N. Jin, M. Chen, L. Guo, Y. Li, and Y. Chen, "Double-vector model-free predictive control method for voltage source inverter with visualization analysis," *IEEE Trans. Ind. Electron.*, vol. 69, no. 10, pp. 10066–10078, Oct. 2022.

Mahdi S. Mousavi received B.Sc. and M.Sc. degrees in electrical engineering from the Iran University of Science and Technology (IUST), Tehran, Iran, in 2013 and 2015, respectively, and the Ph.D. degree in power electronics from Shahid Rajaee Teacher Training University (SRTTU), Tehran, Iran, in 2022.

He is currently collaborating with the Electrical Drives Lab, SRTTU. From 2015 to 2021, he was a Researcher with Niroo Research Institute, Tehran. Since 2021, he has been a Power Electronics Engineer with the Iranian Research Institute of Electrical Engineering (IRIEE), Academic Center for Education, Culture and Research (ACECR) Railway Traction Group. His research interests include variable-speed drives and model predictive control.

Behnam Nikmaram received the B.Sc. degree from the Islamic Azad University-South Tehran Branch, Tehran, Iran, in 2016, and the M.Sc. degree from Shahid Rajaee Teacher Training University, Tehran, Iran, in 2020, both in electrical engineering.

He is currently working with the ACECR Railway Traction Group. From 2020 to 2021, he was collaborating with the Niroo Research Institute as a Research Power Electronics Engineer. His research interests include electric railway traction vehicles, encoderless drives, power electronics and applications, and renewable energy.

Abolfazl Nassaji received the B.Sc. degree in electrical engineering from the University of Kashan, Kashan, Iran, in 2013, and the M.Sc. degree in power electronics from the University of Science and Culture (USC), Tehran, Iran, in 2020.

Since 2019, he has been as a Power Electronics Engineer with the ACECR Railway Traction Group. In this role, he has played a major part in the Research and Development team, contributing to the design and manufacturing of the first domestically produced metro train in Iran. His work focuses on advancing technologies in railway traction systems and sustainable energy solutions. His research interests include power electronics converters, renewable energy systems, and solar energy applications.

S. Alireza Davari (Senior Member, IEEE) received the M.Sc. and Ph.D. degrees in electrical engineering from the Iran University of Science and Technology, Tehran, Iran, in 2006 and 2012, respectively.

From 2010 and 2011, he left for a Sabbatical Visit with Technische Universitaet Muenchen, Munich, Germany. From 2013 and 2020, he was an Assistant Professor with Shahid Rajaee Teacher Training University, Tehran, where he has been an Associate Professor since 2020. Between 2022 and 2023, he was a Visiting Research Professor with Universidad Andres Bello, Santiago, Chile. His research interests include encoder-less drives, predictive control, power electronics, and renewable energy.

Freddy Flores-Bahamonde (Senior Member, IEEE) was born in Osorno, Chile, in 1983. He received the M.Sc. and Ph.D. degrees in electronics engineering from Universitat Rovira i Virgili, Tarragona, Spain, in 2009 and 2013, respectively.

He is currently an Assistant Professor with the Engineering Sciences Department, Universidad Andres Bello, Santiago, Chile, where he is also a Researcher with the Center for Energy Transformation. In 2015, he joined as a Postdoctoral Fellow with the Advanced Center for Electrical and Electronic Engineering (AC3E), Universidad Tecnica Federico Santa Maria (UTFSM), Valparaiso, Chile. In 2017, he was the in charge of the energy area in the technology transfer unit of the AC3E, developing and managing industrial projects related to energy and electric power systems. His main research interests include the design and control of power converters for renewable energies, automotive power systems, and dc microgrids.

Jose Rodriguez (Life Fellow, IEEE) received the engineering degree in electrical engineering from the Universidad Tecnica Federico Santa Maria, Valparaiso, Chile, in 1977, and the Dr.-Ing. degree in electrical engineering from the University of Erlangen, Erlangen, Germany, in 1985.

He has been with the Department of Electronics Engineering, Universidad Tecnica Federico Santa Maria, since 1977, where he was full Professor and President. From 2015 to 2019 he was the President of Universidad Andres Bello, Santiago, Chile. Since 2022, he has been President of Universidad San Sebastian, Santiago, Chile. He has coauthored two books, several book chapters, and more than 700 journal and conference papers. His main research interests include multilevel inverters, new converter topologies, control of power converters, and adjustable-speed drives.

Dr. Rodriguez was the recipient of many best paper awards from journals of IEEE, the National Award of Applied Sciences and Technology from the government of Chile in 2014, and the Eugene Mittelmann Award from the Industrial Electronics Society of IEEE in 2015. From 2014 to 2021, he was included in the list of Highly Cited Researchers published by Web of Science. He is a Member of the Chilean Academy of Engineering.